Science AAAS

Visualizing Individual Nitrogen Dopants in Monolayer Graphene

Liuyan Zhao, *et al.*

Science **333**, 999 (2011);
DOI: 10.1126/science.1208759

Science (print ISSN 0036-8075; online ISSN 1095-9203) is published weekly, except the last week in December, by the American Association for the Advancement of Science, 1200 New York Avenue NW, Washington, DC 20005.

between the two ground states. In most cases (Fig. 4D), one of the modes clearly dominates. However, in some cases (below 10%), both configurations are almost equally populated at the same time. The simultaneous observation of two modes might be due to excitations like the formation of spin domains. Hence, for the first time, our system allows detailed studies on the mechanism of symmetry-breaking in large-scale "magnetic" systems.

A different aspect of our system is revealed when one recalls that the spin configurations actually correspond to local phases of a BEC at different sites of the triangular lattice. This provides new insight into unconventional superfluidity (*21*, *22*): For all phases except the ferromagnetic one, the state corresponds to a superfluid at nonzero quasi-momentum and, thus, nontrivial long-range phase order. Moreover, the observed spiral configurations spontaneously break time-reversal symmetry by showing circular bosonic currents around the triangular plaquettes of the lattice. Clockwise and counterclockwise currents are found in a staggered fashion from plaquette to plaquette. These resemble the currents of the staggered flux state thought to play a role in explaining the pseudogap phase of high-temperature cuprate superconductors (*23*).

Our results demonstrate the realization of a simulator for classical magnetism in a triangular lattice. Let us point out here that these results are obtained simply by using spinless bosons. Due to the high degree of controllability, we succeeded in observing all of the various magnetic phases and phase transitions of first and second order, as well as frustration-induced spontaneous symmetry-breaking. It now becomes possible to quench systems on variable time scales from ferromagnetic to antiferromagnetic couplings and to study the complex relaxation dynamics. Furthermore, extending the studies to the strongly correlated regime promises to give a deeper insight into the understanding of quantum spin models and spin-liquid–like phases (*24*).

References and Notes

1. L. Pauling, *J. Am. Chem. Soc.* **57**, 2680 (1935).
2. G. H. Wannier, *Phys. Rev.* **79**, 357 (1950).
3. L. Balents, *Nature* **464**, 199 (2010).
4. S. Sachdev, *Nat. Phys.* **4**, 173 (2008).
5. R. Moessner, A. P. Ramirez, *Phys. Today* **59**, 24 (2006).
6. D. J. P. Morris *et al.*, *Science* **326**, 411 (2009); 10.1126/science.1178868.
7. T. Fennell *et al.*, *Science* **326**, 415 (2009); 10.1126/science.1177582.
8. M. Lewenstein *et al.*, *Adv. Phys.* **56**, 243 (2007).
9. I. Bloch, J. Dalibard, W. Zwerger, *Rev. Mod. Phys.* **80**, 885 (2008).
10. S. Trotzky *et al.*, *Science* **319**, 295 (2008); 10.1126/science.1150841.
11. K. Kim *et al.*, *Nature* **465**, 590 (2010).
12. X.-S. Ma, B. Dakic, W. Naylor, A. Zeilinger, P. Walther, *Nat. Phys.* **7**, 399 (2011).
13. Y.-J. Lin, R. L. Compton, K. Jiménez-García, J. V. Porto, I. B. Spielman, *Nature* **462**, 628 (2009).
14. W. Zwerger, *Science* **325**, 1507 (2009).
15. J. Simon *et al.*, *Nature* **472**, 307 (2011).
16. C. Becker *et al.*, *N. J. Phys.* **12**, 065025 (2010).
17. A. Eckardt *et al.*, *Europhys. Lett.* **89**, 10010 (2010).
18. Supporting material is available on *Science* Online.
19. A. Eckardt, C. Weiss, M. Holthaus, *Phys. Rev. Lett.* **95**, 260404 (2005).
20. H. Lignier *et al.*, *Phys. Rev. Lett.* **99**, 220403 (2007).
21. G. Wirth, M. Ölschläger, A. Hemmerich, *Nat. Phys.* **7**, 147 (2011).
22. P. Soltan-Panahi, D.-S. Lühmann, J. Struck, P. Windpassinger, K. Sengstock, http://arXiv.org/abs/1104.3456.
23. P. A. Lee, N. Nagaosa, X.-G. Wen, *Rev. Mod. Phys.* **78**, 17 (2006).
24. R. Schmied, T. Roscilde, V. Murg, D. Porras, J. I. Cirac, *N. J. Phys.* **10**, 045017 (2008).

Acknowledgments: We thank A. Rosch, P. Hauke, and D.-S. Lühmann for stimulating discussions and the Deutsche Forschungsgemeinschaft (FOR 801, GRK 1355) and the Landesexzellenzinitiative Hamburg, which is supported by the Joachim Herz Stiftung, for funding. A.E. and M.L. are grateful for support through the Spanish Ministerio de Ciencia y Innovación grant TOQATA, European Research Council grant QUAGATUA, and European Union grants AQUTE and NAMEQUAM.

Supporting Online Material

www.sciencemag.org/cgi/content/full/science.1207239/DC1
SOM Text
Figs. S1 and S2
References

19 April 2011; accepted 8 July 2011
Published online 21 July 2011;
10.1126/science.1207239

Visualizing Individual Nitrogen Dopants in Monolayer Graphene

Liuyan Zhao,[1] Rui He,[1] Kwang Taeg Rim,[2] Theanne Schiros,[3] Keun Soo Kim,[1,4] Hui Zhou,[1]
Christopher Gutiérrez,[1] S. P. Chockalingam,[1] Carlos J. Arguello,[1] Lucia Pálová,[2]
Dennis Nordlund,[5] Mark S. Hybertsen,[6] David R. Reichman,[2] Tony F. Heinz,[1,7] Philip Kim,[1]
Aron Pinczuk,[1,8] George W. Flynn,[2] Abhay N. Pasupathy[1]*

In monolayer graphene, substitutional doping during growth can be used to alter its electronic properties. We used scanning tunneling microscopy, Raman spectroscopy, x-ray spectroscopy, and first principles calculations to characterize individual nitrogen dopants in monolayer graphene grown on a copper substrate. Individual nitrogen atoms were incorporated as graphitic dopants, and a fraction of the extra electron on each nitrogen atom was delocalized into the graphene lattice. The electronic structure of nitrogen-doped graphene was strongly modified only within a few lattice spacings of the site of the nitrogen dopant. These findings show that chemical doping is a promising route to achieving high-quality graphene films with a large carrier concentration.

Substitutional doping is a powerful way to tailor material properties at the nanoscale (*1*), and it might be expected to have fundamentally different consequences when used to alter the electronic properties of inherently two-dimensional (2D) materials such as graphene (*2*). In recent years, several experimental techniques have been developed to dope the carbon lattice (*3*–*9*). These include methods applied during growth of large-area graphene films (*4*, *5*, *7*, *8*) and ways to modify the material after growth (*3*, *6*), as well as a new one-pot procedure to produce highly doped, few-layer graphitic structures (*9*). Several characterization techniques including x-ray photoemission (*10*, *11*), Raman spectroscopy (*3*, *5*, *7*) and transmission electron microscopy (*12*) have been used to analyze the effect of the doping process in graphene. However, a microscopic understanding of the atomic and low-energy electronic structure induced by the substitutional doping process in monolayer graphene is lacking. In our experiment, we used the atomic-resolution imaging capabilities of the scanning tunneling microscope to understand the local structure in the vicinity of a N dopant in monolayer graphene and spectroscopic imaging to measure the density of states and carrier concentration at the nanoscale. We also report scanning Raman spectroscopy, core-level x-ray spectroscopy and first principles calculations to characterize the effect of N-doping on the graphene film.

We grew N-doped graphene films using chemical vapor deposition on copper foil substrates (*13*) in a quartz tube furnace [sample growth details in supporting online material (SOM) I (a)]. Each graphene-covered foil was divided into three parts and immediately studied using Raman spectroscopy, x-ray spectroscopy, and scanning tunneling microscopy (STM) measurements. Samples have been characterized as grown on copper foils as well as after transfer to an insulating SiO_2 substrate [sample transfer and preparation details in SOM I, (b) to (d)].

Raman spectra (Fig. 1A) were taken over large areas (20-μm spot size) of the N-doped

---

[1]Department of Physics, Columbia University, New York, NY 10027, USA. [2]Department of Chemistry, Columbia University, New York, NY 10027, USA. [3]Energy Frontier Research Center, Columbia University, New York, NY 10027, USA. [4]Department of Physics and Graphene Research Institute, Sejong University, Seoul 143-747, Korea. [5]Stanford Synchrotron Radiation Lightsource, SLAC National Accelerator Laboratory, Menlo Park, CA 94025, USA. [6]Center for Functional Nanomaterials, Brookhaven National Laboratory, Upton, NY 11973–5000, USA. [7]Department of Electrical Engineering, Columbia University, New York, NY 10027, USA. [8]Department of Applied Physics and Applied Mathematics, Columbia University, New York, NY 10027, USA.

*To whom correspondence should be addressed. E-mail: pasupathy@phys.columbia.edu

samples on SiO_2 substrates and on a pristine graphene sample for reference. Raman spectra taken on copper-foil substrates showed identical features, along with a luminescence background from the copper [see fig. S1 and SOM II (a)]. The pristine graphene spectrum showed the G and 2D resonances at 1585.5 and 2684.5 cm^{-1} (*14*); little or no signal at the D band at 1348.5 cm^{-1} was observed, indicating a low defect density. In contrast, the doped samples exhibit strong D and D′ resonances (*6*, *15*–*17*), as well as changes in the intensity and position of the G and 2D bands (*18*, *19*). The Raman spectra on N-doped graphene were consistent with the presence of dopants or defects that modify the free carrier concentration while preserving the basic structural properties of the graphene sheet.

We confirmed the presence of N dopants in the graphene lattice by performing x-ray photoelectron spectroscopy (XPS) and near-edge x-ray absorption fine structure (NEXAFS) spectroscopy at the nitrogen K-edge for a pristine and NG10 doped sample (Fig. 1B) [see SOM I (e)]. The addition of NH_3 in the graphene growth resulted in sharp peaks at 400.7 and 408 eV in the NEXAFS spectrum, corresponding to 1s-to-π^* and -σ^* transitions, respectively, for a single molecular species. The sharpness and strong polarization dependence of the peaks indicates that this species has well-defined, in-plane N-C bonds in the graphene lattice. Based on previous studies (*20*–*22*), this peak can be assigned to sp^2-bonded graphitic nitrogen with three C neighbors. Representative N1s XPS shows a higher–binding energy component (black line) for the NH_3-grown samples, indicating the formation of more

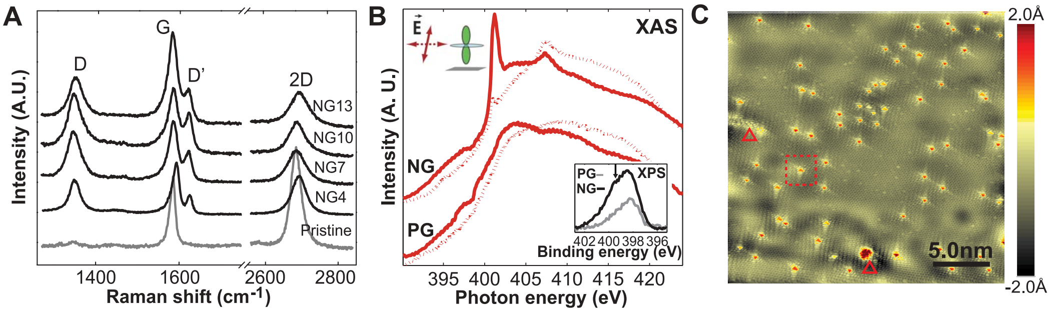

Fig. 1. Raman, XPS, and STM spectra of N-doped graphene. (**A**) Raman spectra taken at pristine and N-doped (four different doping levels) graphene on a SiO_2/Si substrate (20-μm laser spot) showing systematic changes in the spectra as a function of doping. A.U., arbitrary units. (**B**) NEXAFS (total electron yield) of pristine and N-doped graphene on copper foil at the N K-edge. N-doping results in a new peak in the spectrum at 400.7 eV due to graphitic N. XAS, x-ray absorption spectroscopy. (Inset) XPS data for pristine and NG10 graphene, showing a higher–binding energy component (black arrow) for the doped sample. (**C**) Large-area STM image of N-doped graphene on copper foil showing the presence of numerous pointlike dopants (such as the dashed box) and occasional clusters of dopants (indicated by triangles) (V_{bias} = 0.8 V, I_{set} = 0.8 nA).

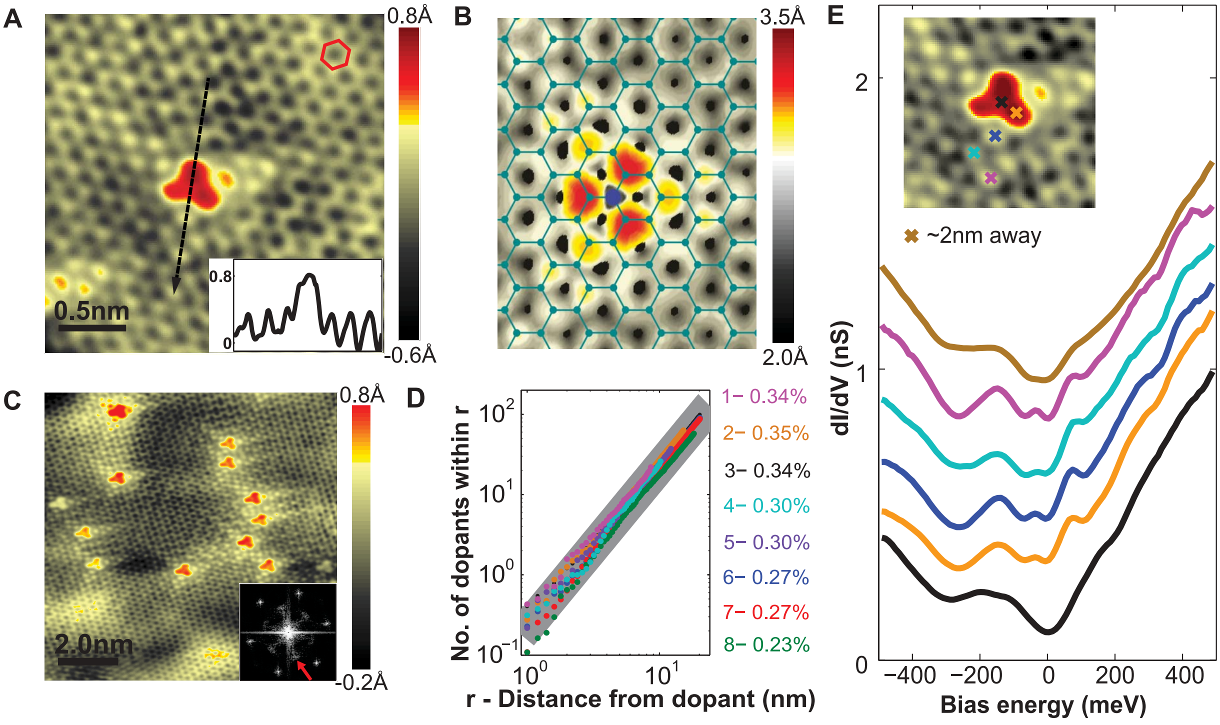

Fig. 2. STM imaging of nitrogen dopants. (**A**) STM image of the most common doping form observed on N-doped graphene on copper foil, corresponding to a single graphitic N dopant. (Inset) Line profile across the dopant shows atomic corrugation and apparent height of the dopant (V_{bias} = 0.8 V, I_{set} = 0.8 nA). (**B**) Simulated STM image of graphitic N dopant (V_{bias} = 0.5 V), based on DFT calculations. Also superposed is a ball-and-stick model of the graphene lattice with a single N impurity. (**C**) STM image of N-doped graphene on copper foil showing 14 graphitic dopants and strong intervalley scattering tails. (Inset) FFT of topography shows atomic peaks (outer hexagon) and intervalley scattering peaks (inner hexagon, indicated by red arrow) (V_{bias} = 0.8 V, I_{set} = 0.8 nA). (**D**) Spatial distribution of N-N distances from eight samples on copper foils with different N concentrations. The distributions are all fit well by a quadratic power law (expected error bands in gray) over all length scales indicating that N dopants incorporate randomly into the graphene lattice. (**E**) *dI*/*dV* curves taken on a N atom (bottom) and on the bright topographic features near the nitrogen atom on N-doped graphene on copper, offset vertically for clarity. The top curve is the *dI*/*dV* spectrum taken ~2 nm away from the dopant. (Inset) Positions where the spectra were taken (V_{bias} = 0.8 V, I_{set} = 1.0 nA).

electronegative N-C bonds in the graphene lattice as opposed to at edges or defects (gray line). This higher–binding energy peak is generally considered a signature of graphitic N in studies of modified carbon films (*6*, *21*, *23*, *24*).

For STM measurements, the graphene-coated substrates were transferred in ambient atmosphere soon after preparation into an ultra-high–vacuum (UHV), low-temperature instrument that is capable of picometer resolution. The treated copper substrates were degassed in UHV at a temperature of 350°C for several hours before STM experiments were performed. Although many areas of the copper foil displayed a rough topography because of polycrystallinity, we occasionally found large areas where atomically flat terraces can be observed. The NG10 samples were optimal for STM studies, because there is a reasonable probability of observing such flat and clean areas along with the dopant features described below; our detailed STM measurements described below are performed on several such samples between 50 and 77 K.

A representative STM topography of N-doped graphene on a large copper terrace (Fig. 1C) mostly revealed the pristine graphene lattice, but the image also showed several bright objects (nearly identical in appearance) with lateral dimensions of a few atomic spacings, consistent with previous measurements on doped films (*9*, *25*). These bright objects were not seen in pristine graphene films (see below), leading us to associate them with N dopants. By simply counting up the number of bright features and associating each with a single N dopant, we arrived at a N doping concentration per carbon atom of 0.34%. Measurements across several similar samples yielded N concentrations between 0.23 and 0.35%.

A close-up topography of one of these doping features (Fig. 2A) revealed three bright spots forming a triangle. The distance between the bright spots was equal to the graphene lattice constant (2.5 Å). Far away from the doping feature, the honeycomb lattice of graphene was recovered. Following the honeycomb lattice through the doping structure situated each of the three bright spots on a C atom of the same sublattice. An STM line scan through the dopant (Fig. 2A, inset) yielded a maximum apparent out-of-plane height of 0.6 ± 0.2 Å and would be consistent with the N atom substituting for a C atom in the plane of the graphene. From sampling areas on several different N-doped graphene samples, we observe that more than 90% of the dopants are of this form. The observed STM image closely matched our simulated STM image (Fig. 2B) computed from the local density of states for graphitic doping where one N atom replaces a single C atom, as well as other recent calculations (*26*). Our STM image simulations were carried out using the Tersoff-Hamann approach (*27*) based on density functional theory (DFT) calculations in the local density approximation for exchange and correlation, with a plane-wave basis set and norm-conserving pseudopotentials as implemented in the Quantum-ESPRESSO package (*28*) [see SOM II (e)]. The calculated STM image shows the brightest features (red spots) on the nearest neighbor C atoms to N (shown in blue). Visible features extended to several lattice spacings from the N, and the overall triangular symmetry of the image matched the experiment.

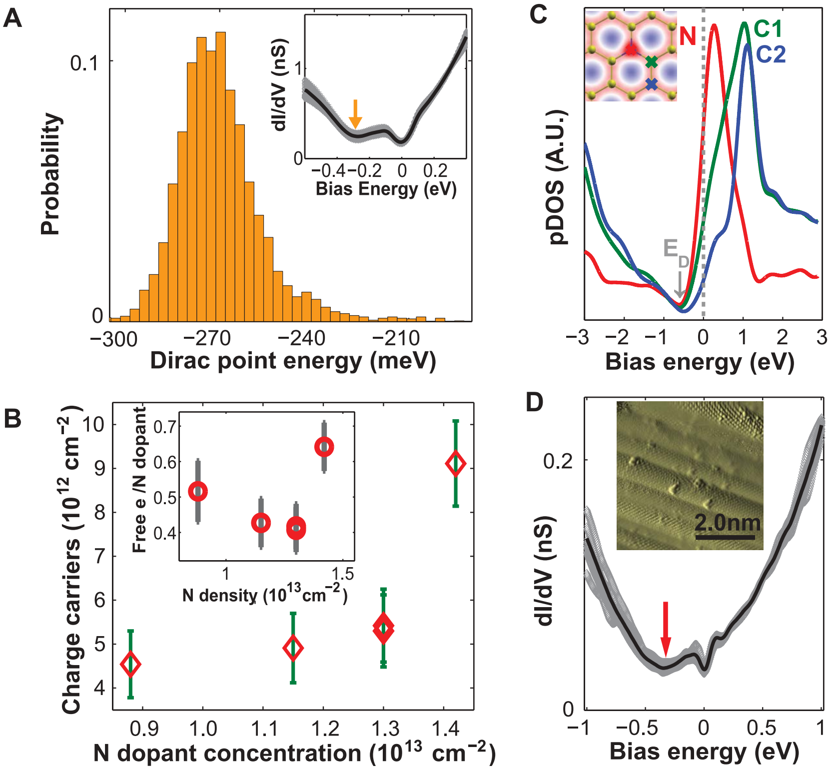

Fig. 3. Spectroscopy and doping in N-doped graphene. (**A**) Histogram of the spatial variation of the Dirac point for N-doped graphene on copper foil over an area of 40 nm by 40 nm ($V_{\mathrm{bias}} = 0.6$ V, $I_{\mathrm{set}} = 1.0$ nA). (Inset) Spatially averaged *dI*/*dV* spectrums (black line) and variation (gray band) over the area. The orange arrow indicates the position of the Dirac point. (**B**) Spatially averaged graphene charge-carrier concentration as a function of average nitrogen concentration level for five different samples measured on N-doped graphene on copper foil. (Inset) Free charge carriers per nitrogen atom for each of these samples. (**C**) Calculated projected density of states near the Fermi energy for a 1% doping level. The gray dashed line denotes the position of the Fermi energy. (Inset) Color plot of the calculated charge density around the N dopant. (**D**) Averaged *dI*/*dV* spectrum for N-doped graphene transferred to a SiO_2/Si substrate (black line) and spatial variation (gray band). The Dirac point is at −330 meV (red arrow) ($V_{\mathrm{bias}} = 1.0$ V, $I_{\mathrm{set}} = 0.1$ nA). (Inset) Topography shown in derivative mode to enhance atomic contrast.

The STM observations show that the majority of the doping occurs via graphitic substitution in these samples [see SOM II (b) and fig. S2 for examples of other doping forms seen]. Larger-area STM images of the samples (such as Fig. 2C) located 14 dopants, all in the graphitic form, which is consistent with the NEXAFS results. Apart from the local structure around each dopant, we also see long "tails" around each dopant. These arise from intervalley electron scattering induced by the N dopant, and similar features have been seen before in other experiments (*29*, *30*). The fast Fourier transform (FFT) of Fig. 2C (inset) shows evidence for this strong scattering. The FFT shows two sets of points arranged in hexagons. Whereas the outer hexagon of points in the FFT corresponds to the atomic lattice, the inner hexagon in this FFT arises from the strong intervalley scattering induced by N dopants (*29*, *30*).

Large-area STM images, such as those in Figs. 1C and 2C, can give us information on whether clustering of dopants occurs during growth. To analyze the possibility of dopant clustering, we used STM images to calculate all of the N-N distances for each sample. Figure 2D shows a histogram of these distances for several different samples on a logarithmic scale. A true random distribution of dopants would imply a quadratic distribution of dopant-to-dopant distances, which we observed in all of our samples down to length scales of a few lattice constants. Nearby dopants preferred to incorporate on the same sublattice of graphene. Indeed, all of the dopants shown in Fig. 2C are located on the same sublattice, and evidence for this phenomenon is seen in other samples as well [see SOM II (c) and fig. S3].

We performed detailed STM spectroscopy measurements of the differential conductance *dI*/*dV* (Fig. 2E) to understand the effect of the

N atoms on the low-energy electronic structure of the graphene film (here, *dI*/*dV* is the derivative of the current with respect to the voltage obtained using a lock-in amplifier). The most prominent features seen in all of the curves, which have been seen previously on monolayer graphene (*31*), are two depressions near zero bias and near –300 meV relative to the tip. The zero-bias feature occurs when energies are too low to excite the optical phonon mode in graphene monolayers that can enhance the tunneling current (*31*). The –300 meV feature occurs near the Dirac point where the density of states of graphene is low (*31*–*33*). We thus associated the dip seen at –270 mV in Fig. 2E with the Dirac point for an electron-doped graphene layer. Measurements of the Dirac point over a 40- by 40-nm area of an NG10 sample show a distribution of values (Fig. 3A). We used the energy of the Dirac point measured at each position of a sample to convert to a charge-carrier density at that location using the relation for the ideal graphene band structure—namely, $n = \frac{E_D^2}{\pi(\hbar v_F)^2}$ (where n is the charge-carrier density, E_D is the Dirac point energy, and $\hbar$ is Planck's constant h divided by 2π). Taking a value for the Fermi velocity $v_F = 10^6$ m/s, we arrive at an average charge-carrier density of $(5.42 \pm 0.83) \times 10^{12}$ electrons per cm^2. We can compare this to the N-doping concentration calculated by simply counting the number of observed dopants in the area where the measurements are performed. The observed N doping in this area corresponds to 0.34% N atoms per C atom or, equivalently, a N atom density of 1.3×10^{13}cm^{-2}. Together with the charge-carrier density measured by STM spectroscopy, this result implies that each graphitic N dopant contributes (on average) ~0.42 ± 0.07 mobile carriers to the graphene lattice. We have performed such detailed spectroscopic measurements across different samples with N atom concentrations varying from 0.23 to 0.35% (Fig. 3B) and found a strong correlation between the number of N dopants and the extracted charge-carrier density. An independent measurement of the carrier concentration based on the shift in the position of the G peak in the Raman spectrum induced by doping (*18*, *19*) was $5 \pm 1.5 \times 10^{12}$ cm^{-2} [see SOM II (d) and fig. S4].

Our DFT calculations (*28*) provide insight to the electrostatic balance between the N dopants and free carriers in the graphene sheet. Focusing on a single, graphitic N dopant, the projected N density of states (pDOS) on the π-system (Fig. 3C) revealed a resonance caused by the N p_z orbital centered 0.3 eV above the Fermi energy (E_F). The pDOS for the C nearest neighbor exhibited a shoulder caused by its electronic coupling to the N, with a reduced shoulder on the next nearest neighbor. The occupied fraction of these resonances represented the localized charge near the N centers. The balancing charge went to the rest of the π states. The Dirac point still appeared in the pDOS, shifted to below E_F, as also seen in our total DOS and in other recent calculations (*26*, *34*). We studied N concentrations (from 0.6 to 5.6%) by varying the super cell size for a single dopant. Using the Dirac point shift in the total DOS as a measure of free electron concentration, we estimate (using the formula above) that 50 to 70% of electrons are delocalized, with oscillations indicative of electronic interference effects in the simulation cells that we used [see SOM II (e) and fig. S5]. A value of ~ 60% would be consistent with the experiment values shown in Fig. 3B.

To draw comparisons with other measurements of doping in graphene films, it is important to understand the effect of the copper-foil substrate on the carrier concentration via charge transfer (*35*, *36*), as well as by changing the charge screening in the graphene layer. We performed STM measurements of pristine graphene films on copper foils and estimated that the doping induced by the copper-foil substrate into the graphene film is <10^{12} electrons/cm^2 [see SOM II (f) and fig. S7]. The copper substrate can also modify the charge screening length in the graphene film. We studied doped graphene films transferred to a SiO$_2$ dielectric substrate (*37*), a process that left residue on or below the graphene surface. Typical STM and atomic force microscopy images displayed surface roughness of a few nanometers, but occasionally we found small regions of the sample where the graphene honeycomb lattice could be resolved. Figure 3C shows the average *dI*/*dV* spectrum taken over one such clean area (the STM image is shown in the inset in the derivative mode to remove the overall roughness of the substrate and enhance the atomic contrast). The overall features in the spectrum are preserved, but now $E_D = -330 \pm 20$ meV ($n = 8 \times 10^{12}$cm^{-2}). The transfer processes, as well as the SiO$_2$ substrate itself, introduce an unknown doping concentration into the film; thus, it is not possible to directly compare the doping level of the two samples. However, the spectrum of doped graphene on SiO$_2$ is broadly consistent with the spectrum of doped graphene on copper foil, indicating the absence of a strong hybridization between the graphene and underlying copper.

The local electronic structure around a N dopant also affects the electronic nature of the doped graphene film. In Fig. 4A, we show spectra obtained on and far away (~2 nm) from a dopant atom. Although the overall features of the spectra were preserved on the N atom, the electron-hole asymmetry in the local density of states was much stronger on the N atom, in accord with DFT calculations (Fig. 3B). The amount of scattering introduced by the dopant can be assessed by

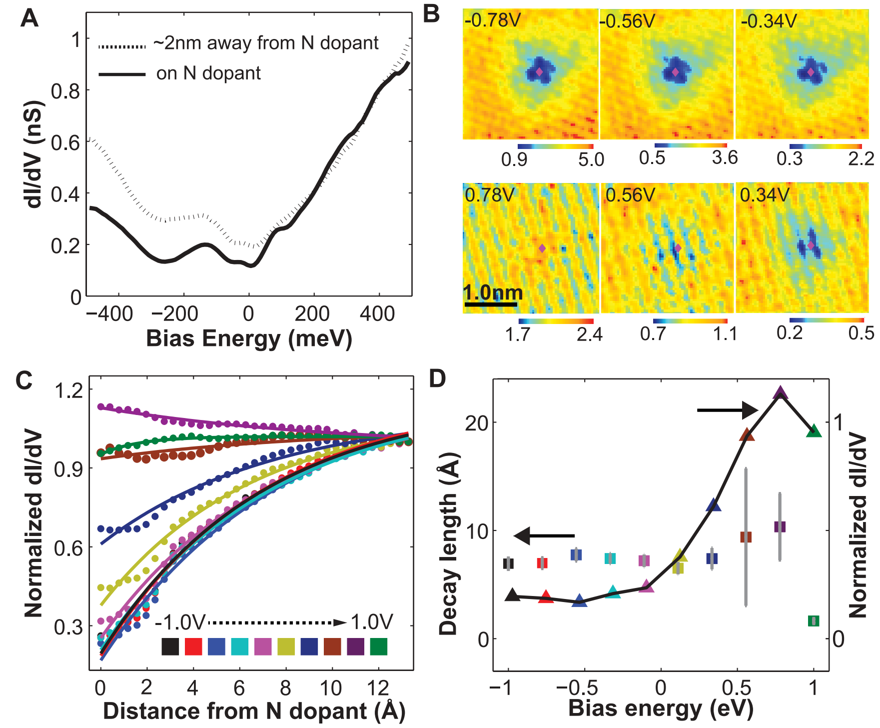

Fig. 4. Spectroscopic mapping around a single N dopant. (**A**) *dI*/*dV* spectra taken on the N atom (solid line) and far away from the N atom (dashed line) for N-doped graphene on copper foil ($V_{bias} = 0.8$ V, $I_{set} = 1.0$ nA). (**B**) STM spectroscopic maps taken in the vicinity of a single N dopant for N-doped graphene on copper foil (dopant position indicated by a dot) at different energies with N positions marked by red diamonds ($V_{bias} = 0.8$ V, $I_{set} = 1.0$ nA). (**C**) Radially averaged differential conductance as a function of the distance from the N atom at different energies, normalized to unity at distances far away from the N atom. The fits are to an exponential decay function. (**D**) Extracted decay lengths for different energies (squares) and the ratio of the differential conductance on the N site to the background (triangles) for different energies. The decay lengths are ~7 Å for all energies.

STM imaging (*29*, *32*, *38*). We performed STM spectroscopic mapping in a 2.5-nm area around one graphitic N dopant (STM junction parameters are $V = 0.8$ V, $I = 1$ nA). Shown in Fig. 4B are a subset of these maps, acquired at bias voltages (applied to the sample relative to the tip) from –0.78 to 0.78 V. The maps did not show much contrast at high positive bias, but the local DOS around the N atom was strongly suppressed at energies below the E_F. The local DOS recovered its background value within a few lattice constants of the dopant atom. We plotted the radial distribution of the dI/dV intensity (Fig. 4C) from the maps in Fig. 4B as a function of distance from the N atom, normalizing the background value of the dI/dV to unity for each energy. The intensity of the spectral weight changes caused by the N dopant were energy-dependent, but the decay lengths were ~7 Å for all energies (Fig. 4D). This result indicates that the electronic perturbation caused by a nitrogen dopant is localized near the dopant atom, which is confirmed in large-area dI/dV maps, and seen in the calculated charge distribution [see SOM II (e) and fig. S5] and simulated STM image in Fig. 2B (*26*).

References and Notes

1. N. W. Ashcroft, N. D. Mermin, *Solid State Physics* (Holt, New York, 1976).
2. A. H. Castro Neto, F. Guinea, N. M. R. Peres, K. S. Novoselov, A. K. Geim, *Rev. Mod. Phys.* **81**, 109 (2009).
3. X. R. Wang *et al.*, *Science* **324**, 768 (2009).
4. I. Gierz, C. Riedl, U. Starke, C. R. Ast, K. Kern, *Nano Lett.* **8**, 4603 (2008).
5. D. C. Wei *et al.*, *Nano Lett.* **9**, 1752 (2009).
6. Y.-C. Lin, C.-Y. Lin, P.-W. Chiu, *Appl. Phys. Lett.* **96**, 133110 (2010).
7. L. S. Panchokarla *et al.*, *Adv. Mater.* **21**, 4726 (2009).
8. Z. Z. Sun *et al.*, *Nature* **468**, 549 (2010).
9. D. Deng *et al.*, *Chem. Mater.* **23**, 1188 (2011).
10. L. T. Qu, Y. Liu, J. B. Baek, L. M. Dai, *ACS Nano* **4**, 1321 (2010).
11. Y. Wang, Y. Y. Shao, D. W. Matson, J. H. Li, Y. H. Lin, *ACS Nano* **4**, 1790 (2010).
12. J. C. Meyer *et al.*, *Nat. Mater.* **10**, 209 (2011).
13. X. Li *et al.*, *Science* **324**, 1312 (2009); 10.1126/science.1171245.
14. A. C. Ferrari *et al.*, *Phys. Rev. Lett.* **97**, 187401 (2006).
15. M. S. Dresselhaus, A. Jorio, A. G. Souza Filho, R. Saito, *Philos. Trans. R. Soc. A Math. Phys. Eng. Sci.* **368**, 5355 (2010).
16. A. Jorio *et al.*, *J. Phys. Condens. Matter* **22**, 334204 (2010).
17. M. M. Lucchese *et al.*, *Carbon* **48**, 1592 (2010).
18. J. Yan, Y. B. Zhang, P. Kim, A. Pinczuk, *Phys. Rev. Lett.* **98**, 166802 (2007).
19. A. Das *et al.*, *Nat. Nanotechnol.* **3**, 210 (2008).
20. I. Shimoyama, G. Wu, T. Sekiguchi, Y. Baba, *Phys. Rev. B* **62**, R6053 (2000).
21. N. Hellgren *et al.*, *Thin Solid Films* **471**, 19 (2005).
22. N. Hellgren *et al.*, *Appl. Phys. Lett.* **79**, 4348 (2001).
23. X. Li *et al.*, *J. Am. Chem. Soc.* **131**, 15939 (2009).
24. S. Point, T. Minea, B. Bouchet-Fabre, A. Granier, G. Turban, *Diamond Relat. Mater.* **14**, 891 (2005).
25. M. Endo, T. Hayashi, S. H. Hong, T. Enoki, M. S. Dresselhaus, *J. Appl. Phys.* **90**, 5670 (2001).
26. B. Zheng, P. Hermet, L. Henrard, *ACS Nano* **4**, 4165 (2010).
27. J. Tersoff, D. R. Hamann, *Phys. Rev. B* **31**, 805 (1985).
28. P. Giannozzi *et al.*, *J. Phys. Condens. Matter* **21**, 395502 (2009).
29. G. M. Rutter *et al.*, *Science* **317**, 219 (2007).
30. E. Cockayne *et al.*, *Phys. Rev. B* **83**, 195425 (2011).
31. Y. B. Zhang *et al.*, *Nat. Phys.* **4**, 627 (2008).
32. Y. B. Zhang, V. W. Brar, C. Girit, A. Zettl, M. F. Crommie, *Nat. Phys.* **6**, 74 (2010).
33. G. H. Li, A. Luican, E. Y. Andrei, *Phys. Rev. Lett.* **102**, 176804 (2009).
34. A. Lherbier, X. Blase, Y. M. Niquet, F. Triozon, S. Roche, *Phys. Rev. Lett.* **101**, 036808 (2008).
35. G. Giovannetti *et al.*, *Phys. Rev. Lett.* **101**, 026803 (2008).
36. P. A. Khomyakov *et al.*, *Phys. Rev. B* **79**, 195425 (2009).
37. K. S. Kim *et al.*, *Nature* **457**, 706 (2009).
38. A. Deshpande, W. Bao, F. Miao, C. N. Lau, B. J. LeRoy, *Phys. Rev. B* **79**, 205411 (2009).

Acknowledgments: This material is based on work supported as part of the Center for Re-Defining Photovoltaic Efficiency Through Molecule Scale Control, an Energy Frontier Research Center funded by the U.S. Department of Energy (DOE), Office of Science, Office of Basic Energy Sciences under award no. DE_SC0001085. Support was also provided by the Air Force Office of Scientific Research under grant no. FA9550-11-1-0010 (A.N.P); by the DOE under grants DE-FG02-88ER13937 (G.W.F) and DE-FG02-07ER15842 (T.H.) for research carried out in part at the Center for Functional Nanomaterials, Brookhaven National Laboratory, contract no. DE-AC02-98CH10886 (M.S.H.) and at the National Synchrotron Light Source, contract no. DE-AC02-98CH10886; by the Office of Naval Research under Graphene Multidisciplinary University Research Initiative (A.P. and P.K.); by the Defense Advanced Research Projects Agency Carbon Electronics for RF Applications program (P.K.); by the NSF under grant no. CHE-0641523 (A.P.); by the New York State Office of Science, Technology and Academic Research and by the Priority Research Centers Program (2011-0018395) through the National Research Foundation of Korea funded by the Ministry of Education, Science and Technology (K.S.K.). Equipment and material support was provided by the NSF under grant CHE-07-01483 (G.W.F.). Portions of this research were carried out at the Stanford Synchrotron Radiation Lightsource (SSRL), a Directorate of SLAC National Accelerator Laboratory and an Office of Science User Facility operated for the DOE Office of Science by Stanford University. We thank C. Jaye and D. Fischer for assistance in using National Synchrotron Light Source beamline U7A, H. Ogasawara for assistance at SSRL beamline 13-2, and C. Marianetti and D. Prezzi for useful discussions. The authors declare no competing financial interests. Requests for materials should be addressed to A.N.P.

Supporting Online Material

www.sciencemag.org/cgi/content/full/333/6045/999/DC1
Materials and Methods
SOM Text
Figs. S1 to S7

23 May 2011; accepted 29 June 2011
10.1126/science.1208759

Guided Growth of Millimeter-Long Horizontal Nanowires with Controlled Orientations

David Tsivion,[1] Mark Schvartzman,[1] Ronit Popovitz-Biro,[2] Palle von Huth,[2] Ernesto Joselevich[1]*

The large-scale assembly of nanowires with controlled orientation on surfaces remains one challenge preventing their integration into practical devices. We report the vapor-liquid-solid growth of aligned, millimeter-long, horizontal GaN nanowires with controlled crystallographic orientations on different planes of sapphire. The growth directions, crystallographic orientation, and faceting of the nanowires vary with each surface orientation, as determined by their epitaxial relationship with the substrate, as well as by a graphoepitaxial effect that guides their growth along surface steps and grooves. Despite their interaction with the surface, these horizontally grown nanowires display few structural defects, exhibiting optical and electronic properties comparable to those of vertically grown nanowires. This paves the way to highly controlled nanowire structures with potential applications not available by other means.

Semiconductors with controlled structures are at the core of the most advanced technologies in our everyday life, but defects induced by stress during growth often degrade the electronic and optical properties. For example, single-crystal gallium nitride was first produced in 1969 by epitaxial growth on sapphire (*1*), but it took three decades of research to reduce its defect concentration before it became the basis of the blue light-emitting diodes (LEDs) and violet lasers that enabled outdoor TV screens and the Blu-ray disk. The vapor-liquid-solid (VLS) growth method, first described in 1964 (*2*), has attracted overwhelming renewed attention during the past decade (*3*), as a means of producing stress-free single-crystal semiconductor nanowires with unparalleled electronic and optical properties suitable for ultraminiaturized electronics (*4*), optoelectronics (*5*), renewable energy (*6*), and chemical and biological sensing (*7*). Yet the large-scale assembly of horizontal nanowires with controlled orientation on surfaces remains a challenge toward their integration into practical devices. To this end, several assembly processes have been devised, including the use of liquid flows (*8*), electric fields (*9*),

---

[1] Department of Materials and Interfaces, Weizmann Institute of Science, Rehovot 76100, Israel. [2] Chemical Research Support, Weizmann Institute of Science, Rehovot 76100, Israel.

*To whom correspondence should be addressed. E-mail: ernesto.joselevich@weizmann.ac.il